Corrosion Science 253 (2025) 112944

Contents lists available at ScienceDirect

Corrosion Science

journal homepage: www.elsevier.com/locate/corsci

Oxidation behavior and failure mechanism of NiCoCrAl eutectic multi-principal element alloys co-doped with Y and Hf at 1100 °C and 1200 °C

Aihui Huang [a], Chao Yang [b,*], Xuanzhen Liu [a], Han Zhang [a], Fangwei Guo [a], Bingnan Qian [c], Jie Lu [a,*], Xiaofeng Zhao [a], Paul K. Chu [d]

[a] Shanghai Key Laboratory of Advanced High-Temperature Materials and Precision Forming, School of Materials Science and Engineering, Shanghai Jiao Tong University, Shanghai 200240, China
[b] National Engineering Research Center of Light Alloy Net Forming, Shanghai Jiao Tong University, China
[c] National Key Laboratory of Nuclear Reactor Technology, Nuclear Power Institute of China, Chengdu 610213, China
[d] Department of Physics, Department of Materials Science & Engineering, and Department of Biomedical Engineering, City University of Hong Kong, Tat Chee Avenue, Kowloon, Hong Kong, China

ARTICLE INFO

Keywords:
High-temperature oxidation
Eutectic multi-principal element alloy
Failure mechanism
Oxidation resistance

ABSTRACT

This study investigates the oxidation behavior of Y/Hf co-doped NiCoCrAl-type EMPEAs with various Co and Cr concentrations ($Ni_{59.6}Co_{10}Cr_{10}Al_{20.4}$, $Ni_{50.7}Co_{15}Cr_{15}Al_{19.3}$ and $Ni_{33.4}Co_{25}Cr_{25}Al_{16.6}$ in at%) at 1100 °C and 1200 °C. After oxidation at 1100 °C, increasing Co and Cr contents enhances Y/Hf solubility in the β phase, which delays the θ- to α-Al_2O_3 phase transformation and promotes the formation of larger columnar grains of α-Al_2O_3 scale, thereby reducing the oxidation rate by up to 62 %. After oxidation at 1200 °C, the NiCoCrAl-type EMPEAs with higher Co and Cr content show significantly better spallation resistance due to the reduction of the coefficient of thermal expansion (CTE) and Y/Hf solubility in the γ phase. This reduction minimizes residual stress in the oxide scale and decreases the tendency for oxide intrusion at the scale/alloy interface, thereby enhancing the interfacial fracture energy. These findings provide scientific guidance for optimizing the composition of NiCoCrAl EMPEAs to enhance oxidation resistance in high-temperature applications.

1. Introduction

NiCoCrAlY alloys are extensively utilized as bond coating materials for thermal barrier coatings (TBCs) and overlay coatings in aero-engine and gas turbines due to their excellent oxidation resistance at elevated temperatures [1–3]. The oxidation resistance of NiCoCrAlY alloys relies on the formation of a stable and well-adherent Al_2O_3-based scale with a slow growth rate at high temperatures. Reactive elements (REs) such as Y, Hf, and Zr are commonly incorporated into the substrate to suppress the formation of interfacial voids and inhibit the outward diffusion of Al ion, thereby enhancing scale adhesion and reducing the growth rate of oxide scale [4–6]. However, commercial NiCoCrAlY alloys or coatings (Amdry 365-2, Ni-23Co-17Cr-12Al-0.5Y in wt%) fail to provide adequate oxidation resistance at a high temperature (above 1100 °C) owing to their high oxide scale growth rate and accelerated interfacial degradation, leading to the spallation of oxide scale and shorter service life [7]. This limitation underscores the need for developing novel materials with superior high-temperature oxidation resistance.

Recently, eutectic multi-principal element alloys (EMPEAs) have emerged as a promising candidate for high-temperature applications because of their excellent high-temperature stability and the ability to form a lamellar or rod-like ultra-fine eutectic microstructure with high rupture strength and resistance to high-temperature creep [8–11]. Moreover, the ultra-fine eutectic microstructure plays a critical role in homogenizing the distribution of REs. By optimizing the RE effect, it can minimize the formation of interfacial imperfections (e.g., RE-rich inclusions), thereby enhancing interfacial toughness and oxidation resistance [12,13]. It has been reported that commercial NiCoCrAlY coatings deposited by laser powder deposition and laser cladding exhibit a finer microstructure (like ultra-fine eutectic microstructure) compared to those fabricated by air plasma spray (APS) or high-velocity air-fuel (HVAF) techniques [14–16]. This ultra-fine microstructure promotes the

* Corresponding authors.
E-mail addresses: chaoyang0315@163.com (C. Yang), lu-jie@sjtu.edu.cn (J. Lu).

https://doi.org/10.1016/j.corsci.2025.112944
Received 12 March 2025; Accepted 13 April 2025
Available online 14 April 2025

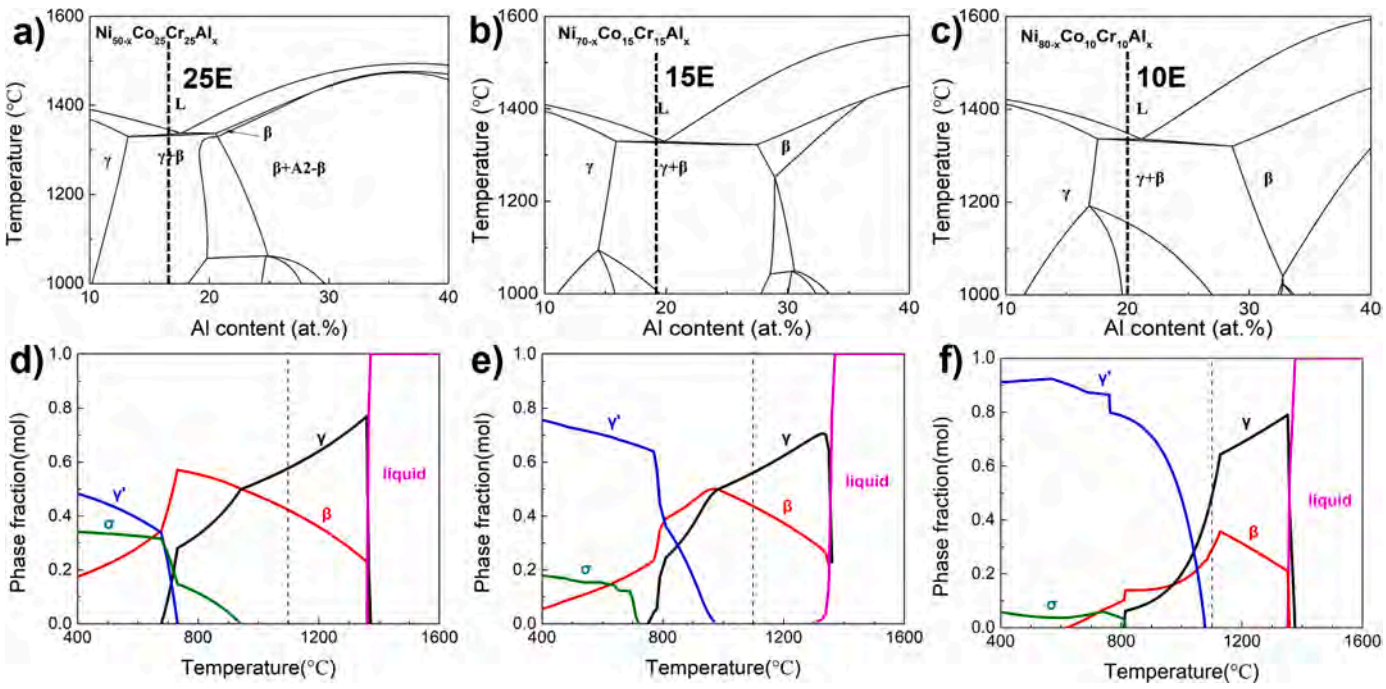

Fig. 1. Thermodynamic calculations of the $Ni_{50-x}Co_{25}Cr_{25}Al_x$, $Ni_{70-x}Co_{15}Cr_{15}Al_x$, and $Ni_{80-x}Co_{10}Cr_{10}Al_x$ systems: (a–c) Pseudo-quaternary phase diagrams with the three alloy compositions shown in the diagram (black dash line); (d-f) Phase fractions of 25E, 15E, and 10E alloys as a function of temperature.

Table 1
Chemical composition of the 25E, 15E, and 10E alloys determined by ICP-OES analysis (in wt%).

Alloys	Elements						
	Ni	Co	Cr	Al	Y	Hf	S
25E	37.8	28.4	25.1	8.6	0.041	0.085	< 0.0005
15E	58.0	16.9	14.9	9.9	0.038	0.087	< 0.0005
10E	67.7	11.4	10.1	10.7	0.043	0.084	< 0.0005

rapid formation of a continuous Al_2O_3 scale and accelerates the transformation from θ-Al_2O_3 to α-Al_2O_3, leading to superior oxidation resistance. Despite the promising benefits offered by these eutectic structures, the oxidation mechanisms and RE interplay with the ultra-fine microstructure in NiCoCrAl-type EMPEAs remain insufficiently understood, warranting further investigation.

To date, various computational approaches, including the calculation of phase diagram (CALPHAD) method [17], simple mixing [18], mixing enthalpy [19], and grouping and machine learning [20], have been developed to design EMPEAs. Herein, three NiCoCrAl-type EMPEAs with different Co and Cr concentrations ($Ni_{59.6}Co_{10}Cr_{10}Al_{20.4}$, $Ni_{50.7}Co_{15}Cr_{15}Al_{19.3}$ and $Ni_{33.4}Co_{25}Cr_{25}Al_{16.6}$) are designed using the CALPHAD method and their oxidation behavior at 1100 °C and 1200 °C is carefully studied. The REs (Y/Hf) are incorporated into the substrate to enhance the scale adhesion. The microstructure of the alloys and their oxide scale oxidation rates, residual stress, and RE solubility are systematically determined to elucidate the oxidation behavior and failure mechanisms. Our findings provide scientific insights into the design of oxidation-resistant NiCoCrAl-type EMPEAs for advanced applications.

2. Materials and method

2.1. Compositional design

The NiCoCrAl-type EMPEAs are designed by deriving the pseudo-quaternary phase diagrams (Fig. 1**a–c**) of the $Ni_{50-x}Co_{25}Cr_{25}Al_x$, $Ni_{70-x}Co_{15}Cr_{15}Al_x$, and $Ni_{80-x}Co_{10}Cr_{10}Al_x$ systems using the CALPHAD method and thermo-calc (TC) software. The actual eutectic point of these systems is ~ 1 at% less than the calculated eutectic point due to non-equilibrium effects during the solidification process [21]. In the computational model, the minor Y and Hf are excluded from the calculation because of the low concentrations (Y: 0.025 at%, Hf: 0.025 at %). According to our previous work [22], the minor Y and Hf shows negligible influence on the types and fractions of primary phases due to their small amounts. Subsequently, three NiCoCrAl-type EMPEAs are generated by the CALPHAD method and designated as 25E, 15E, and 10E according to the Co and Cr concentrations. Table 1 summarizes the chemical compositions of the three alloys, which is determined by inductively coupled plasma optical emission spectra (ICP-OES) analysis. Since the oxidation behavior of the Y/Hf co-doped $Ni_{60-x}Co_{20}Cr_{20}Al_x$ system has been studied by us [22], it will not be discussed in this paper. The phase fraction of the EMPEAs calculated by the TC software (Fig. 1**d–f**) shows a combination of γ and β phases at 1100–1200 ℃.

2.2. Materials preparation and isothermal oxidation test

The 25E, 15E, and 10E alloys were prepared by adding high-purity Y and Hf (> 99.9 wt%) melted in a Ti-gettered high-purity argon atmosphere. The as-cast ingots were remelted five times and subsequently heat treated at 1100 °C for 20 h under an argon atmosphere to ensure

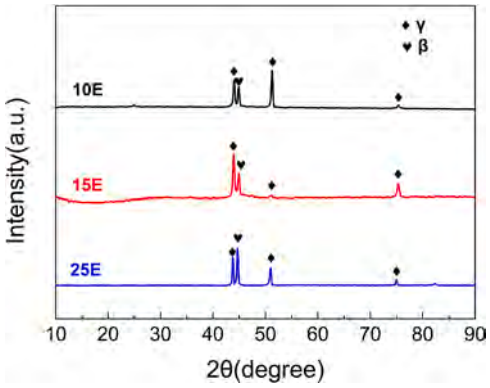

Fig. 2. XRD patterns of the 10E, 15E, and 25E alloys, showing the phase structure.

compositional homogeneity. Square plates (10 × 10 × 2.5 mm^3) were cut from the ingot by a precision cut-off machine (Accutom 5, Struers). The samples were then ground with 5000-grit SiC paper and cleaned in an ultrasonic bath for 5 min. The isothermal oxidation tests were conducted at 1100 °C and 1200 °C in a furnace for up to 500 h. Because of the non-hermetically sealed nature of the chamber furnace, the oxidation atmosphere inside the furnace can be considered the same as the ambient air (21 % oxygen, 78 % nitrogen, and small amounts of other gases such as carbon dioxide and argon). Each composition of NiCoCrAl-type EMPEAs was subjected to three parallel experiments to ensure the reliability and reproducibility of the results. The specimens were removed from the furnace and air-cooled for 10 min with the help of a fan.

2.3. Characterization

The phase structure of the three alloys was determined by X-ray diffraction (XRD, Bruker D8 ADVANCE) at a scanning rate of 5°/min and 2θ scanning range of 10–90°.

The enthalpies of the endothermic reactions of these three NiCoCrAl EMPEAs were measured by differential scanning calorimetry (DSC, Discovery SDT 650, TA Instruments, USA). Scanning electron microscopy (SEM, Mira3, Tescan), energy-dispersive X-ray spectroscopy (EDS, Oxford Instruments), and electron backscatter diffraction (EBSD, Oxford Instruments NordlysMax3) were employed to analyze the microstructure and composition of the alloys and oxide scales. To protect the cross-sectional samples during analysis, a layer of Ni was electroplated onto the oxide scale. Scanning transmission electron microscopy (STEM, Talos F200X G2, Thermo Fisher Scientific, USA) combined with EDS was used to determine the chemical composition. The average coefficient of thermal expansion (CTE) was measured on a high-temperature dilatometer (DIL 402 Expedis Select/Supreme, NETZSCH, Germany) in argon from 25 °C to 1250 °C at a heating rate of 5 °C/min. The specimen for CTE measurements had a rectangular shape with dimensions of 15 × 3 × 3 mm^3. To measure the residual stress in the oxide scales, photoluminescence piezospectroscopy (PLPS) was performed on a confocal Raman microprobe (LabRAM HR, Horiba Jobin Yvon, France) equipped with a 532 nm Nd:YAG laser by Eq. (1) [23], derived from the piezospectroscopic shift of the R2 line in α-Al_2O_3.

$$\Delta\nu = 5.07\sigma \quad (1)$$

Where $\Delta\nu$ is the peak shift of R2 line with respect to that of the stress-free sapphire. The spectra were analyzed by mixed Gaussian-Lorentzian functions (Labspec software) to determine the peak positions. PLPS was also used to identify the phase transformation of Al_2O_3 during the early oxidation stage of these alloys.

Table 2
Chemical compositions (at%) of the β and γ phases in the alloys based on the average of four analyses.

Elements	25E		15E		10E	
	β	γ	β	γ	β	γ
Ni	37.2 ± 1.3	30.6 ± 1.6	50.2 ± 2.5	49.6 ± 1.9	55.9 ± 2.5	54.7 ± 2.1
Co	20.6 ± 0.9	28.2 ± 1.5	12.5 ± 1.4	17.1 ± 1.0	8.8 ± 0.4	13.3 ± 1.7
Cr	13.8 ± 1.0	28.8 ± 1.1	8.8 ± 0.5	19.9 ± 1.6	6.6 ± 0.7	15.7 ± 1.4
Al	28.4 ± 1.9	12.4 ± 0.3	28.5 ± 1.7	13.4 ± 0.8	28.7 ± 2.4	15.3 ± 1.0

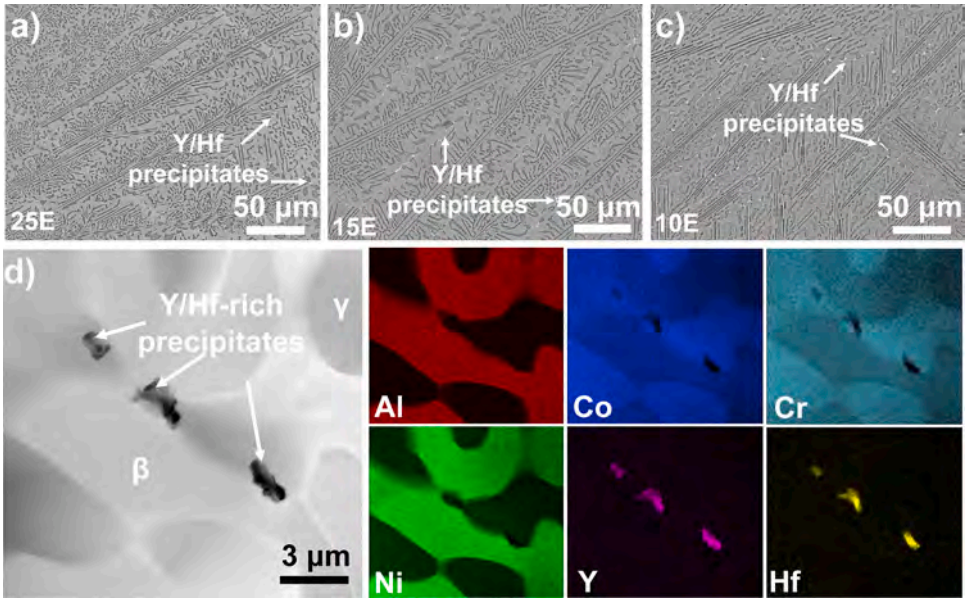

Fig. 3. Microstructural analysis of the 25E, 15E, and 10E alloys: (a-c) Low-magnification BSE images of NiCoCrAl-type EMPEAs (white arrows indicating Y/Hf-rich precipitate); (d) STEM-DF image and EDS maps of the Y/Hf precipitate in the 10E alloy.

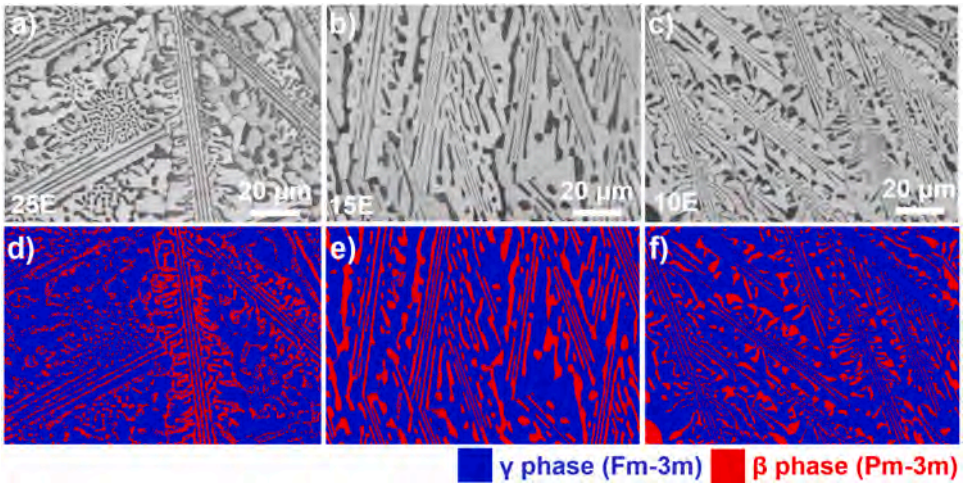

Fig. 4. EBSD analysis of the 25E, 15E, and 10E alloys: (a–c) Band contrast maps and (d–f) Phase maps.

Table 3
Volume fractions of the γ phase and β phase in the alloys based on 5 analyses at a magnification of 2000 ×.

Alloys	γ phase fraction	β phase fraction
25E	64.8 ± 2.0 %	35.2 ± 1.6 %
15E	70.1 ± 2.1 %	29.9 ± 2.7 %
10E	74.7 ± 2.4 %	25.3 ± 1.8 %

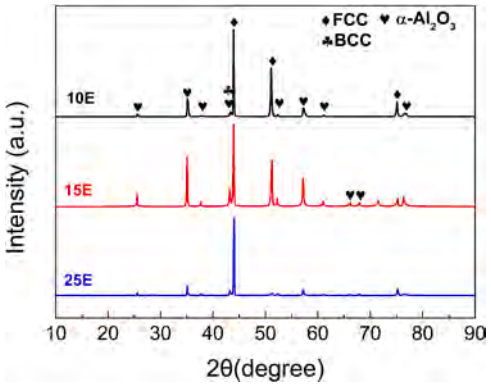

Fig. 5. XRD patterns of the 10E, 15E, and 25E alloys after oxidation for 500 h at 1100 ℃, showing exclusive formation of α-Al_2O_3.

3. Results

3.1. Microstructure of the 25E, 15E and 10E alloys

Fig. 2 indicates that all alloys have a dual-phase microstructure consisting of γ and β phases, consistent with the calculated results (Fig. 1**d–f**). Fig. 3**a–c** reveal that the alloys have a lamellar and rod-like eutectic microstructure comprising the γ phase (bright contrast) and β phase (dark contrast). Moreover, the DSC results show a single sharp endothermic peak during the heating process for each alloy (Fig. S1), which provides strong evidence that these alloys are eutectic as designed. Table 2 provides the composition details of the γ phase and β phase in the alloys, disclosing that the γ phase is enriched in CoCr while the β phase is enriched in NiAl. Moreover, minor Y/Hf precipitates are observed (white contrast in Fig. 3**a–c**). The Y/Hf precipitate (1–2 μm) is confirmed by STEM and EDS mapping, with a composition of approximately 20 % Y, 60 % Hf, and 20 % Ni (in at%) (Fig. 3**d**). Fig. 4 shows that the volume fraction of the β phase decreases with Co and Cr concentrations from 35.2 % to 25.3 % (Table 3). Based on EBSD analysis, the lamellar eutectic microstructure has an average β phase size of approximately 0.5–1 μm, while the rod-like eutectic microstructure shows β phase sizes ranging from 1 μm to 3 μm.

3.2. Oxidation behavior of 25E, 15E, and 10E at 1100 °C

Fig. 5 shows that the oxidation products consist of exclusively α-Al_2O_3 after oxidation at 1100 ℃. Fig. 6 presents the surface morphologies of 25E, 15E, and 10E after 500 h oxidation at 1100 ℃. All the alloys show a uniform and well-adherent α-Al_2O_3 scale without spallation (Fig. 6**a–c**). The α-Al_2O_3 scale formed on the γ and β phases exhibit different surface morphologies possibly due to compositional discrepancy. Meanwhile, the grain size of the α-Al_2O_3 scale formed on the β phase is significantly larger than that formed on the γ phase (Fig. 6**d–f**). Furthermore, the oxide surface on 10E contains more Y/Hf-rich oxides in both the γ and β phases than in 25E and 15E (Fig. 6**f**). Fig. 7 depicts the cross-sectional morphology and elemental distributions after oxidation for 500 h at 1100 ℃. Continuous and uniform α-Al_2O_3 scales are formed on the surface without interfacial imperfections such as pores and oxide intrusions at the scale/alloy interface (Fig. 7**a–c**). The thicknesses of the α-Al_2O_3 scale on 25E, 15E, and 10E are 3.3 μm, 4.2 μm, and 5.3 μm (Fig. 7**d–f**), respectively. These results suggest that the oxidation rate of Y/Hf co-doped NiCoCrAl-type EMPEA can be lowered by increasing the Co and Cr concentrations.

To obtain more information about the oxidation mechanism, Fig. 8 displays the fractured microstructures of the oxide scales formed on the three alloys after 500 h oxidation at 1100 ℃. The oxide scales have the typical double-layer structure consisting of outer equiaxed grains and inner columnar grains (Fig. 8**a, d**, and **g**). It is generally accepted that the outer equiaxed grain is the consequence of the counter-diffusion of Al and O while the formation of columnar grains is dominated by inward O diffusion [24]. The small ratio of equiaxed to columnar grains (Table 4) indicates that inward O diffusion is predominantly in the Al_2O_3 scale growth. Quantitative image analysis of the oxide grain imprints indicates that the average width of the columnar grains decreases with increasing Co and Cr concentrations, ranging from ~ 0.40 μm to ~ 0.75 μm (Fig. 8**b–c, e–f,** and **h–i**).

3.3. Oxidation kinetics of 25E, 15E, and 10E at 1100 °C

Fig. 9 shows the evolution of the oxide scale thickness with oxidation time. The linear fit of the oxide scale thickness to the square root of the oxidation time indicates that oxidation of the three alloys follows the parabolic law [25]. The parabolic rate constant k_h can be obtained by

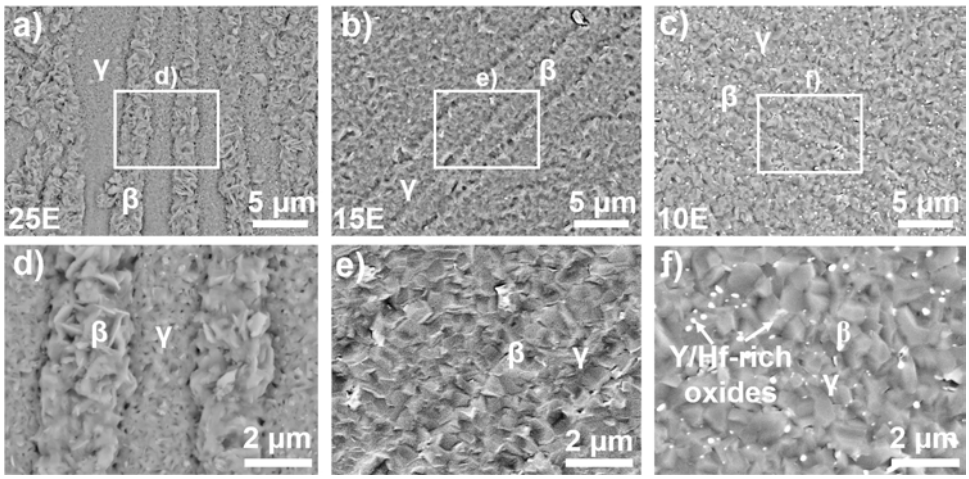

Fig. 6. Surface morphology of 25E, 15E, and 10E after oxidation for 500 h at 1100 ℃: (a–c) Low-magnification BSE images showing the oxide surface; (d–f) High-magnification BSE images showing the detailed morphology of the β and γ phases.

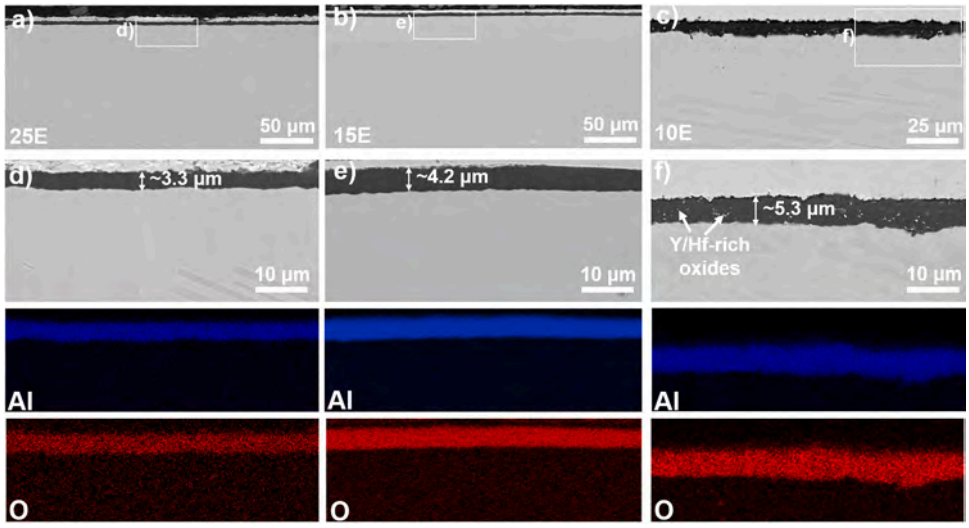

Fig. 7. Cross-sectional morphology and elemental distributions of 25E, 15E, and 10E after oxidation for 500 h at 1100 ℃: (a–c) Low-magnification BSE images; (d–f) High magnification BSE images and corresponding EDS maps showing the composition of OXIDE SCALE.

the following relationship [26]:

$$h_t^2 = k_h t \tag{2}$$

where h_t represents the oxide scale thickness after a given oxidation time t. The parabolic rate constants k_h of 10E, 15E and 25E are estimated to be 14.1×10^{-14} $cm^2 s^{-1}$, 9.5×10^{-14} $cm^2 s^{-1}$, and 5.3×10^{-14} $cm^2 s^{-1}$, respectively. Compared to 10E, 25E exhibits a reduction of ~ 62 % in the parabolic rate constant (k_h) while 15E shows a reduction of ~ 33 %. Although our previous study reported that the $Ni_{40}Co_{20}Cr_{20}Al_{20}$ alloy shows lower oxidation rate than NiCoCrAl EMPEAs after oxidation at 1100 °C [22], this alloy does not possess a eutectic microstructure. The lower oxidation rate of this alloy is attributed to its high β phase volume fraction (~ 65 %) and favorable elemental distribution. In contrast, the present study focuses on the NiCoCrAl-type EMPEAs with a consistent eutectic microstructure and comparable β phase volume fractions (~ 25–35 %). These results reveal that, under a fixed eutectic framework, the Co and Cr concentrations of NiCoCrAl-type EMPEAs play an important role in the oxidation kinetics.

3.4. Oxidation behavior of 25E, 15E, and 10E at 1200 °C

The spallation resistance of the oxide scale becomes increasingly critical when the oxidation temperature rises to 1200 ℃ and surpasses the oxidation kinetics. The spallation degree of the oxide scale is shown in Fig. 10. Spalled areas were distinguished from intact areas using grayscale thresholding of Image J analysis, with darker spalled regions separated from brighter intact oxide scale. Specifically, it decreases from ~ 37 % for the 10E alloy to ~ 5 % for the 25E alloy after 500 h oxidation, suggesting that larger Co and Cr concentrations enhance the spallation resistance of the oxide scale in the NiCoCrAl-type EMPEAs at 1200 °C. The surface and cross-sectional morphologies of the oxide scales on these alloys after oxidation at 1200 ℃ are examined. These results provide valuable comparative information on the oxidation resistance of the alloys. Although mass gain measurements were not conducted in this study, they will be considered in future work to provide a more comprehensive understanding of the oxidation kinetics, particularly regarding internal oxidation and spallation.

Fig. 11 presents the surface morphology of the three alloys after oxidation for 100 h at 1200 °C. In the case of the 10E and 15E alloys,

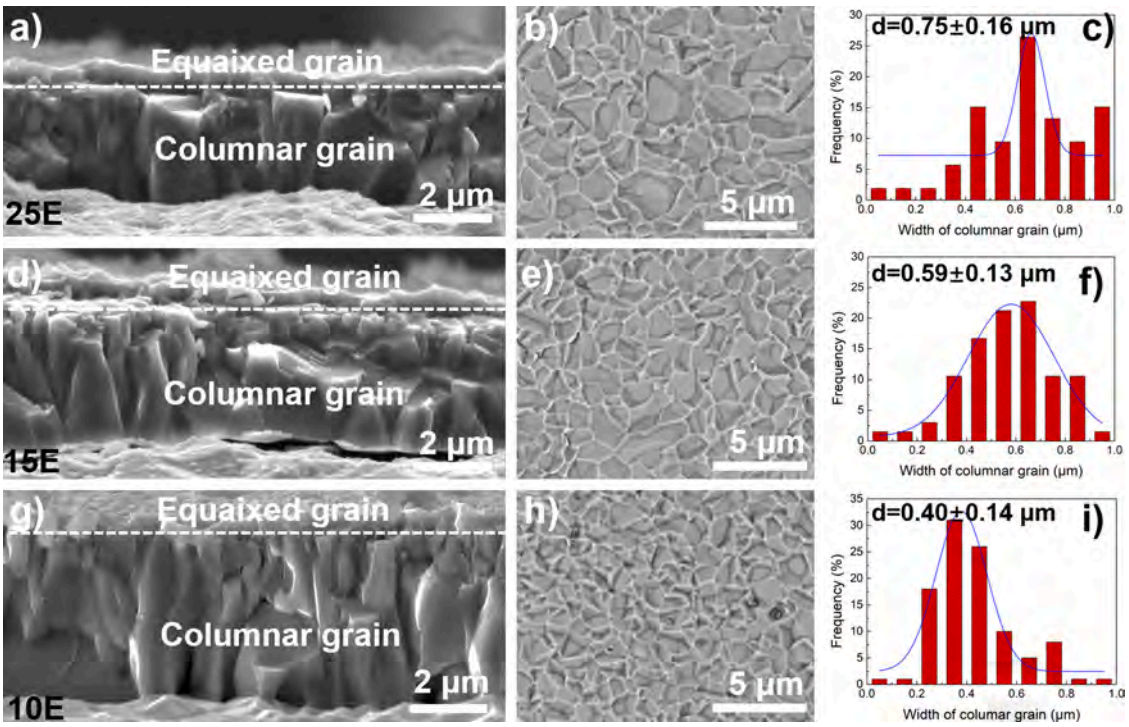

Fig. 8. Microstructural analysis of the OXIDE SCALEs: (a–c) 25E, (d-f) 15E, and (g–i) 10E after oxidation for 500 h at 1100 ℃: (a, d, g) SE images showing the fractured cross-sectional microstructures of OXIDE SCALEs (white dash lines delineate the boundaries between the equiaxed grains and columnar grains); (b, e, h) SE images showing the imprints left on the substrates by the columnar α-Al_2O_3 grains; (c, f, i) Distributions of widths of the columnar grains quantified from their imprints (b, e, h). The fractured cross-sectional microstructures of the OXIDE SCALEs are obtained by the mechanical fracture test.

Table 4
Variation of the ratios of the equiaxed grain to columnar grain in the alloys.

Alloys	Ratios of the equiaxed grain to columnar grain
25E	6.4 ± 1.0 %
15E	7.7 ± 1.1 %
10E	8.2 ± 1.4 %

substantial amounts of oxide intrusion surround the Y/Hf-rich oxides at the spallation region (Fig. 11**a–f**). With regard to the 25E alloy, finer Y/Hf-rich oxides are uniformly distributed at the grain boundaries of the α-Al_2O_3 scale without oxide intrusions and oxide scale spallation (Fig. 11**g–i**). However, oxide intrusions are not observed after oxidation at 1100 ℃, suggesting that the formation of oxide intrusions cannot stem from the over-doping of REs (Y/Hf) [27]. At an elevated temperature of 1200 °C, the diffusion rates of Y and Hf to the scale/alloy interface along phase boundaries increase. Additionally, the rapid coarsening of the γ and β phases at this temperature reduces the number of sites available for Y and Hf distribution in the alloy. These two factors give rise to the localized enrichment of Y/Hf precipitates at the grain and phase boundaries during prolonged oxidation to facilitate the formation of oxide intrusions. The distribution of Y/Hf precipitates is consistent with the location of oxide intrusions (Fig. S2), also indicating that the distribution of Y/Hf precipitates plays an important role in oxide intrusions in the NiCoCrAl-type EMPEAs.

Fig. 12 shows the cross-sectional morphology and elemental distributions of the three alloys after oxidation for 250 h at 1200 ℃. BSE-EDS mapping reveals the presence of oxide intrusions and Y/Hf-rich oxides in the spallation region near the scale/alloy interface in 10E and 15E (Fig. 12**a–f**), consistent with the surface morphology of these alloys. The results reveal a strong correlation between the spallation regions and oxide intrusions at the scale/alloy interface of 10E and 15E. In contrast,

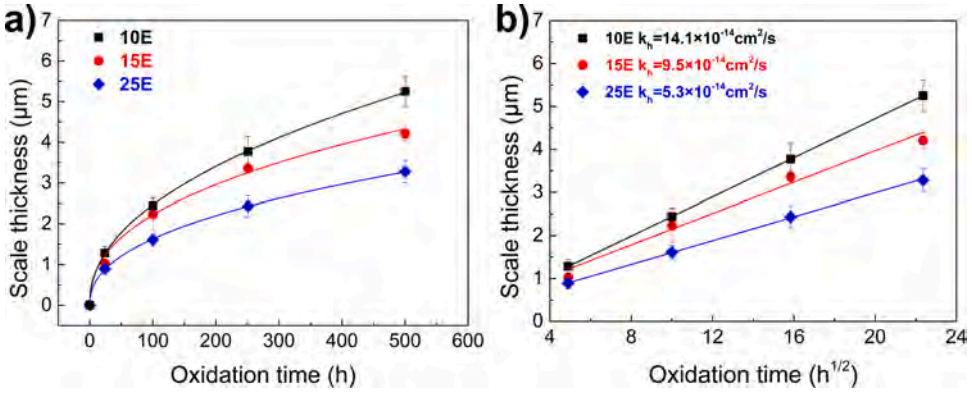

Fig. 9. Oxidation kinetics of 25E, 15E, and 10E at 1100 ℃: (a) Thicknesses of the oxide scales as a function of oxidation time; (b) Thicknesses of the oxide scales on as a function of the square root of oxidation time, showing the parabolic law.

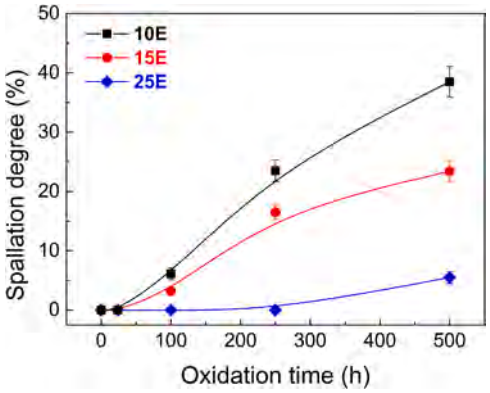

Fig. 10. Spallation degree of oxide scales as a function of oxidation time at 1200 °C determined by the ratio of the spalled area to the total area of the oxide scale, measured by the Image J software from five 50 × magnification BSE images for the three different samples.

no oxide intrusions are observed from the scale/alloy interface of 25E after 250 h oxidation at 1200 ℃ (Fig. 12**g–i**). However, minor oxide intrusions are detected surrounding Y/Hf-rich oxides in the spalled regions of the oxidized surface on 25E after oxidation for 500 h at 1200 ℃ (Fig. 13**a–c**). Interfacial pores are observed near the oxide intrusions (Fig. 13**d–f**), potentially related to volume shrinkage associated with the transformation of α-Al_2O_3 to $Y_3Al_5O_{12}$ [28]. Overall, the formation of oxide intrusions at the scale/alloy interface plays a critical role in determining the spallation resistance of the alloys at 1200 ℃, and it is predominantly influenced by the distribution of REs-rich oxides during oxidation.

4. Discussion

The oxidation resistance of NiCoCrAl-type EMPEA can be enhanced by increasing the Co and Cr concentrations (Fig. 8). Here, we discuss the mechanism responsible for the different oxidation resistance of NiCoCrAl-type EMPEAs at 1100 °C and 1200 °C.

4.1. NiCoCrAl-type EMPEAs at 1100 °C

After oxidation at 1100 ℃, the oxidation rate of NiCoCrAl-type EMPEAs decreases with Co and Cr concentrations. Fig. 9 and Table 3 show that the oxidation rates of the three NiCoCrAl-type EMPEAs depend on the growth of columnar grains and inward oxygen diffusion is the primary factor controlling the oxidation rate. The segregation of REs (Y/Hf) ions to the grain boundaries of the Al_2O_3 scale can inhibit the outward diffusion of Al from the underlying alloy [29]. As a result, oxygen diffusion becomes the dominant mechanism for the growth of the Al_2O_3 scale. Therefore, the oxidation rates are governed by the effective diffusivity of oxygen (D_o^{eff}), which is determined by the lattice and grain boundary diffusion of oxygen [30,31]:

$$D_o^{eff} = fD_o^{gb} + (1-f)D_o^{L} \tag{3}$$

where f represents the volume fraction of grain boundary diffusion, D_o^{gb} and D_o^{L} are the grain boundary diffusion and lattice diffusion of oxygen, respectively. Owing to the significantly larger value of D_o^{gb} than D_o^{L} (about 3–4 orders of magnitude higher), the expression for D_o^{eff} can be approximated as [32]:

$$D_o^{eff} \approx fD_o^{gb} = \frac{2\delta}{d}D_o^{gb} \tag{4}$$

where δ is the width of grain boundary (about 1 nm [33]), d is the width of columnar grain.

Fig. 14**a** illustrates the relationship between D_o^{eff} and the width of the columnar grain by setting D_o^{gb} according to the literature [31], showing a decreasing trend with increasing d. For columnar grain widths of 0.40 μm, 0.59 μm, and 0.75 μm in the case of $\delta D_o^{gb} = 7.5 \times 10^{-8}$ μm^3/s, D_o^{eff} of 10E, 15E and 25E is calculated to be 3.5×10^{-7} μm^3/s, 2.6×10^{-7} μm^3/s, and 1.6×10^{-7} μm^3/s, respectively. To better understand the

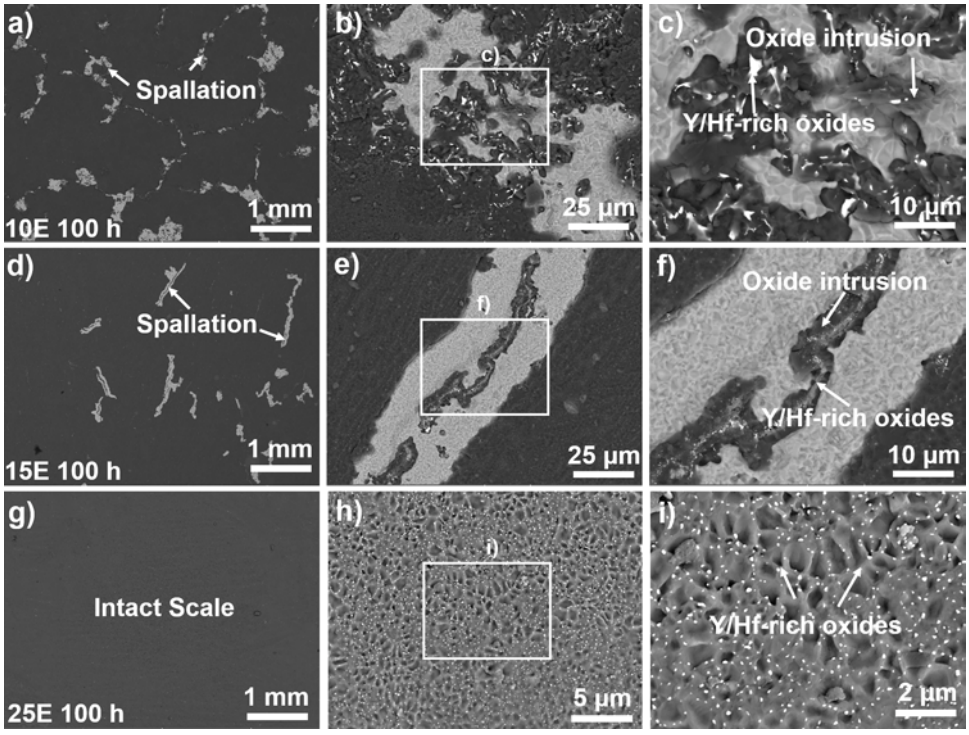

Fig. 11. Surface morphologies of (a–c) 10E, (d–f) 15E, and (g-i) 25E after oxidation for 100 h at 1200 ℃: (a, d, g) Low-magnification BSE images showing the oxide scale; (b, e, h) and (c, f, i) High-magnification BSE images showing the morphology of the oxide scale.

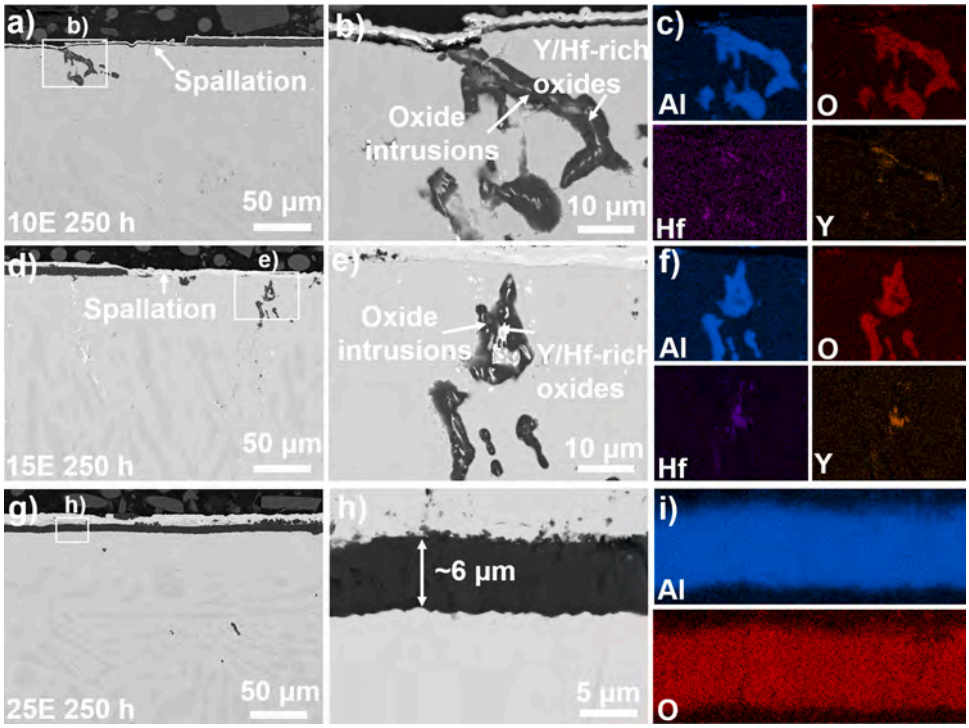

Fig. 12. Cross-sectional morphology and elemental distributions of (a–c) 10E, (d-f) 15E, and (g–i) 25E after oxidation for 250 h at 1200 °C: (a, d, g) Low-magnification BSE images showing the cross-sectional microstructure; (b, e, h) High-magnification BSE images and (c, f, i) EDS elemental maps showing the composition of the oxide scale.

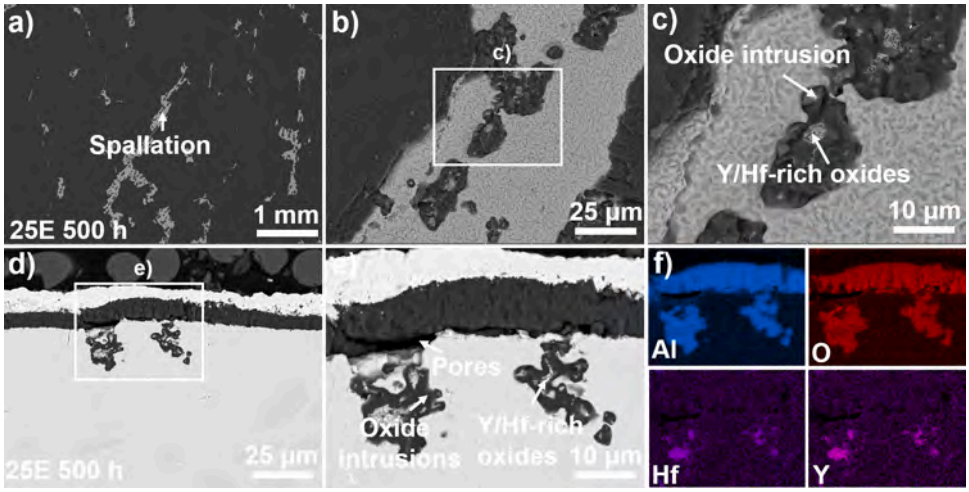

Fig. 13. Surface and cross-sectional morphology of 25E after oxidation for 500 h at 1200 °C: (a) Low-magnification BSE image showing the oxide scale; (b–c) High-magnification BSE images showing the oxide intrusion and Y/Hf-rich oxides in the spallation region; (d) Low-magnification and (e) High-magnification BSE images and (f) Elemental maps of the oxide scale.

effect of oxygen diffusion on the oxidation rate, Fig. 14**b** compares the decreasing rates of D_o^{eff} and k_h of 15E and 25E relative to 10E. The reduction rate of D_o^{eff} is consistent with that of the oxidation rate, confirming that the difference in the oxidation rate is attributed to the columnar grain widths.

Although the oxidation rates of three alloys are not abnormally high in the initial stage (Fig. 9**a**), the θ- to α-Al_2O_3 phase transformation is important for the grain size of α-Al_2O_3 owing to its critical effect on the nucleation sites [34]. The accelerated θ- to α-Al_2O_3 phase transformation can increase the number of sites for nucleation of α-Al_2O_3, which results in a smaller Al_2O_3 grain [35]. For instance, the NiCrAl alloy has higher oxidation rate than NiAl alloy because the chromium accelerates the phase transformation, and thus formed the fine grained α-Al_2O_3 [36]. Moreover, the θ-Al_2O_3 phase is formed on the alloys during the initial oxidation stage and is controlled by outward Al diffusion [37]. The Al diffusion coefficients of the γ and β phases are calculated by the TC software (Table 5). The Al diffusion coefficients of the β phase are significantly higher than those of the γ phase, suggesting that θ-Al_2O_3 should be formed on the surface of the β phase in agreement with the literature [22,38].

It is well recognized that the θ- to α- alumina transformation occurs rapidly at 1100 °C [], making it difficult to characterize the intermediate

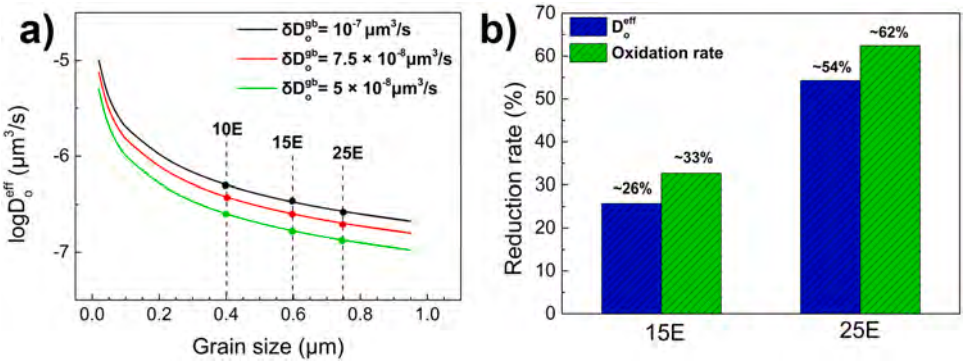

Fig. 14. (a) Evolution of the effective diffusivity of oxygen (D_o^{eff}) as a function of the width of columnar grains. The average value of the width of columnar grains is obtained from Fig. 6. (b) Reduction rate of D_o^{eff} and oxidation rates of 15E and 25E alloy in comparison with that of 10E.

Table 5
Al diffusion coefficients of the γ and β phases at 1100 ℃ calculated by the TC software.

Alloys	D_{Al}^{β}(cm^2/s)	D_{Al}^{γ}(cm^2/s)
25E	2.66×10^{-10}	9.68×10^{-14}
15E	2.49×10^{-10}	9.54×10^{-14}
10E	1.82×10^{-10}	9.37×10^{-14}

Table 6
θ-Al_2O_3 concentrations in the oxide scale of each alloy after oxidation for 5 min at 1100 ℃.

Alloys	θ-Al_2O_3 content in the whole oxide scale (wt%)
25E	14.1 ± 2.0 %
15E	6.5 ± 1.1 %
10E	1.3 ± 1.4 %

oxide phases through conventional post-oxidation analysis. Therefore, the PLPS spectra are collected after oxidation for 5 min to determine the phase constitution of θ-Al_2O_3 on the β phase of the three alloys (Fig. 15**a–c**). Based on the PLPS results and Eq. (5), the concentrations of θ-Al_2O_3 (wt%) on the β phase of 10E, 15E, and 25E are 6 %, 13 %, and 40 %, respectively:

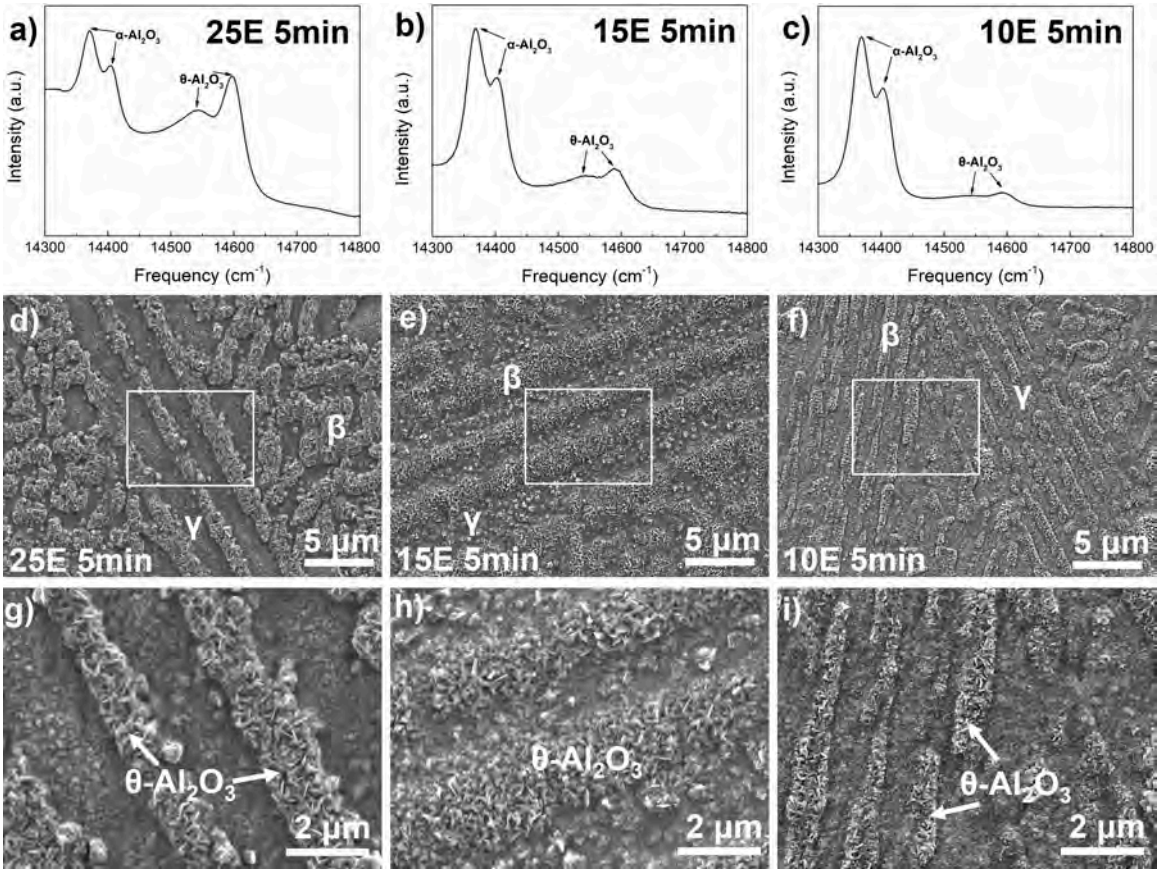

Fig. 15. PLPS spectra and microstructure of the Al_2O_3 scale on 25E, 15E, and 10E after oxidation for 5 min at 1100 ℃: (a–c) PLPS curves of the Al_2O_3 scale formed on the β phase; (d–f) Low-magnification SE images showing the surface morphology; (g–i) High-magnification SE images, showing the θ-Al_2O_3 morphology on the β phase.

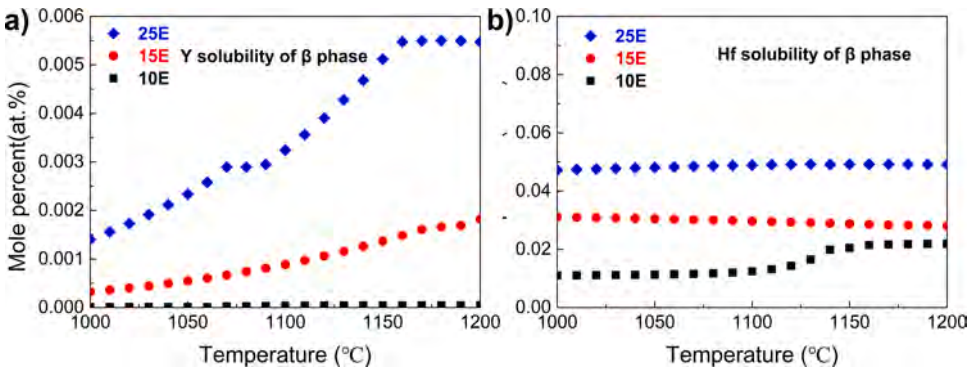

Fig. 16. The Y and Hf solubility of the β phase in NiCoCrAl-type EMPEAs at 1000–1200 ℃ by the TC software.

Table 7
Y and Hf solubility of the β phase at 1100 ℃ calculated by the TC software.

Alloys	Y(at%)	Hf (at%)
25E	3.24×10^{-3}	0.049
15E	8.87×10^{-4}	0.029
10E	3.50×10^{-5}	0.013

$$C_\theta = \frac{A_{14575} + A_{14645}}{A_{14402} + A_{14432} + A_{14575} + A_{14645}} \quad (5)$$

where A denotes the area of the peaks (calculated by the deconvolution integration method), and the subscript represents the peak wavenumber. SEM indicates that the θ-Al_2O_3 (needle-like morphology in Fig. 15**g–i**) is formed on the β phase. Hence, the concentration of θ-Al_2O_3 in the oxide scale can be estimated by multiplying the calculated θ-Al_2O_3 concentration by the volume fraction of the β phase. The concentration of θ-Al_2O_3 shows increase trend as the Co and Cr content increases, from 1.3 % for 10E alloy to 14.1 % for 25E alloy (Table 6). Consequently, the larger grain size of the columnar grain in the 15E and 25E alloys can be attributed to the larger concentrations of θ-Al_2O_3 during the early oxidation stage leading to a smaller oxidation rate.

Since the difference of the phase fraction of the β phase is not significant, the high θ-Al_2O_3 concentration should be attributed to other factors. According to the literature [39–41], REs (Y/Hf) can delay the phase transformation from θ- to α-Al_2O_3 in NiCoCrAlY and NiAlHf by entering the θ-Al_2O_3 lattice during the early oxidation stage. It is reported that Cr promote this phase transformation, acting as a "third element" that facilitates nucleation [42]. For instance, the addition of Cr to the NiAl alloy significantly promote the formation of α-Al_2O_3 [36]. In contrast, Co likely delays this transformation by stabilizing the θ-Al_2O_3 phase owing to the structural similarity between CoO and θ-Al_2O_3 (cubic structure) [43]. However, as the θ-Al_2O_3 forms exclusively on the β phase and not on the γ phase, the high θ-Al_2O_3 concentration is primarily driven by β phase-related factors, such as Y/Hf stabilization, with alloying effect (Co and Cr) playing secondary roles.

Therefore, the solubility of Hf and Y in the β phase has been calculated and is detailed in Fig. 16. As Co and Cr concentrations increases in NiCoCrAl-type EMPEAs, the solubility of Hf in the β phase rises from 3.50×10^{-5} at% in the 10E alloy to 3.24×10^{-3} at% in the 25E alloy, and that of Y increases from 0.013 at% to 0.049 at% (Table 7). Although the solubility of Y cannot be determined accurately due to the strong tendency of the formation of Ni-Y intermetallic compounds [44,45], it follows a similar trend to that of Hf (Fig. 16). Eventually, the higher Y and Hf solubility of the β phase in NiCoCrAl-type EMPEAs is the primary reason for the larger θ-Al_2O_3 concentration during the early oxidation stage, thereby resulting in smaller oxidation rates for 15E and 25E at 1100 ℃.

It is noteworthy that the Al content in the 25E alloy is ~ 4 at% lower than 10E alloy, which is similar to the Al content difference reported in our previous study [22]. In that work, the reduction in Al content led to a substantial decrease in the β phase volume fraction (from 15.3 % in $Ni_{44}Co_{20}Cr_{20}Al_{16}$ alloy to 65.2 % in $Ni_{40}Co_{20}Cr_{20}Al_{20}$ alloy) and significantly affected the oxidation rate. However, in the present study, despite the Al content difference, all three NiCoCrAl EMPEAs show nearly identical β phase volume fractions. These results suggest that, compared with Al content alone, the volume fraction of the β phase plays a more dominant role in influencing the oxidation rate of NiCoCrAl-type alloys. Therefore, Fig. 17**a** shows the relationship between the β phase fraction and oxidation rate of NiCoCrAl-type alloys for the same Y/Hf concentration (0.025 at%). Although there is a general increase in the oxidation rate with decreasing β phase fraction, the relationship lacks a well-defined and consistent correlation, suggesting that other factors may also contribute to the oxidation rates. Prior studies have noted the importance of valence electron concentration (VEC) on the volume fractions of the β and γ phases [46–48]. For instance, increasing the Al

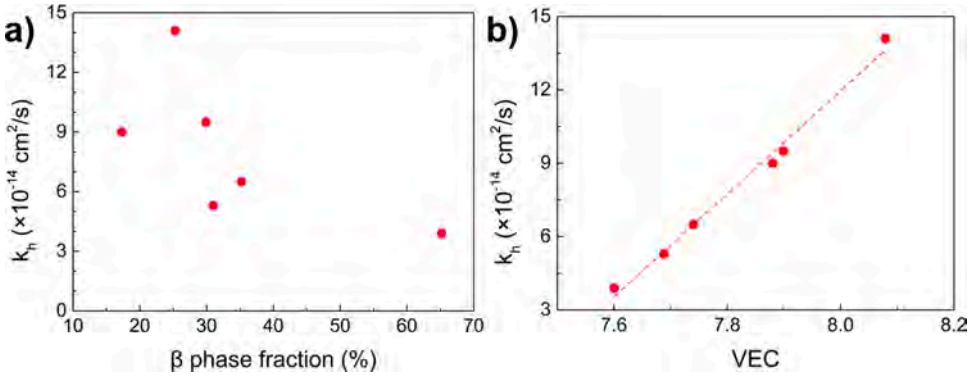

Fig. 17. (a) Relationship between the β phase fraction and oxidation rates; (b) VEC and oxidation rates of Y/Hf co-doped NiCoCrAl-type alloys at 1100 ℃ based on this study and Ref. [22].

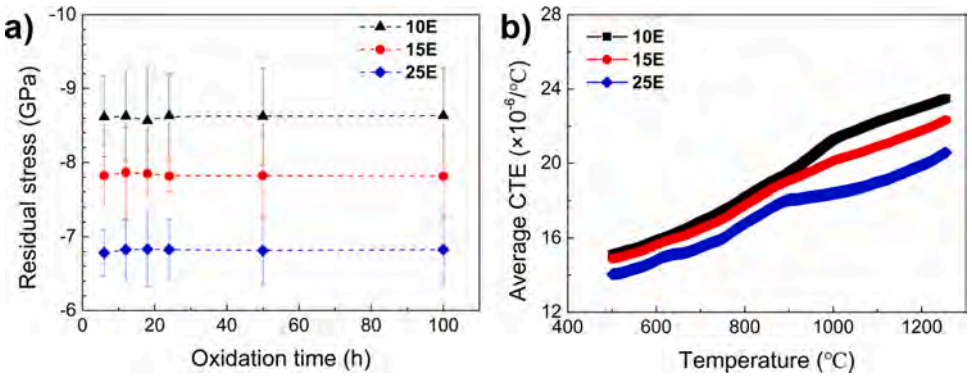

Fig. 18. (a) Evolution of the residual stress in the Al_2O_3 scale of 10E, 15E, and 25E with oxidation time; (b) Evolution of the average CTE as a function of temperature up to 1250 ℃. The average residual stress is based on 100 measurements, and the error bar shows the standard error.

concentration in Al_xCoCrFeNi high entropy alloys decreases VEC but increases the β phase fraction [48]. Fig. 17**b** shows the scatter diagram of the relationship between VEC and oxidation rates of NiCoCrAl-type alloys, revealing a well-defined and consistent correlation. VEC is a crucial factor affecting the oxidation rates of NiCoCrAl-type alloys at 1100 ℃ and the underlying mechanism requires further studies in the future.

4.2. Spallation resistance of Al_2O_3 scale of NiCoCrAl-type EMPEAs at 1200 °C

After oxidation at 1200 °C, the spallation resistance of the Al_2O_3 scale is improved together with increasing Co and Cr concentrations (Fig. 10). Spallation of the oxide scale occurs typically when the elastic strain energy in the oxide scale exceeds the interfacial fracture energy (G_c) as expressed below [49,50]:

$$\frac{(1-\nu^2)}{2E}\sigma^2 h > G_c \tag{6}$$

where ν and E represent the Poisson's ratio and the elastic modulus of the Al_2O_3 scale and σ and h denote the residual stress and thickness of the Al_2O_3 scale, respectively. Therefore, the interfacial fracture energy, residual stress, and thickness of the Al_2O_3 scale play crucial roles in determining the resistance to spallation. According to Fig. 12 and Fig. S2, the thickness of the Al_2O_3 scale is nearly the same (6.0–6.5 μm) for all the alloys after oxidation for 250 h at 1200 ℃. Therefore, the effects of Al_2O_3 scale thickness and oxidation kinetic are negligible.

The evolution of residual stress in the intact oxide scale region is shown in Fig. 18**a** after oxidation at 1200 ℃. The residual stress of the Al_2O_3 scale decreases with increasing Co and Cr concentrations, from − 8.6 GPa of 10E to − 6.8 GPa of 25E. The residual stress of the oxide scale at room temperature comprises two components: thermal mismatch stress (σ_T) and growth stress (σ_g) [51]. The thermal mismatch stress (σ_T) arises from the difference in CTE between the alloy and Al_2O_3 scale, while the growth stress (σ_g) is generated by the lateral growth of the Al_2O_3 scale. Assuming that the creep relaxation is negligible due to the fast-cooling process, σ_T and σ_g can be calculated by the following equations [52]:

$$\sigma_T = \frac{E_{ox}}{1-\nu_{ox}}(\alpha_{ox}-\alpha_m)\Delta T \tag{7}$$

$$\sigma_g = \frac{E_{ox}^T}{(1-\nu_{ox})}\left[\frac{\sigma_{ox}(1-\nu_{ox})}{E_{ox}} - \frac{(\alpha_{ox}-\alpha_m)\Delta T}{1+R}\right] \tag{8}$$

$$R = \frac{E_{ox}(1-\nu_m)h_{ox}}{E_m(1-\nu_{ox})h_m} \tag{9}$$

where E_{ox} and ν_{ox} are the elastic modulus and Poisson's ratio of the Al_2O_3 scale at room temperature, E_{ox}^T is the elastic modulus of Al_2O_3 scale at 1200 °C, α_{ox} and α_m are the CTE of Al_2O_3 scale and substrate alloy, and h_{ox} and h_m are the thickness of the Al_2O_3 scale and substrate alloy, respectively.

Table 8
Calculated thermal mismatch stress and growth stress of 25E, 15E, and 10E alloys.

Alloys	Thermal mismatch stress (GPa)	Growth stress (GPa)
25E	− 6.8	− 0.19
15E	− 7.9	− 0.22
10E	− 8.6	− 0.21

In order to calculate the thermal mismatch stress and growth stress, Fig. 18**b** shows the evolution of CTEs of the three alloys as a function of temperature up to 1250 °C. The average CTE of 10E, 15E, and 25E from the room temperature to 1200 ℃ is 23.0×10^{-6}/°C, 21.7×10^{-6}/℃ and 19.8×10^{-6}/℃, respectively. By substituting the parameters into Eqs. (7)–(9) (E_{ox}=380 GPa, E_{ox}^T=330 GPa, α_{ox}= 8×10^{-6}/℃, ν_{ox}= 0.2, R ≈ 0 for $h_m \gg h_{ox}$) [51], Table 8 presents the thermal mismatch stress and growth stress of the three alloys. The thermal mismatch stress decreases with increasing Co and Cr concentrations, dropping from − 8.6 GPa for 25E to − 6.8 GPa for 10E. The growth stress of these alloys is nearly the same about − 0.21 GPa. Therefore, the variation of the residual stress in these alloys is ascribed to the difference CTE of these three alloys. According to the reported data [53], the β-phase alloys possess lower CTE than γ-phase alloys at a high temperature. Moreover, it is reported that increasing the Co content can also reduce the CTE of NiCoCrAl-type and AlCoCrFeNi-type alloys [54–56]. Eventually, the low CTE of 25E can be ascribed to its higher volume fraction of the β phase and Co content.

The interfacial fracture energy is primarily influenced by two factors: impurity segregation at the scale/alloy interface and the presence of interfacial imperfections (e.g., interfacial pores and oxide intrusion) [57,58]. The distribution of REs plays a critical role in determining the interfacial impurity levels. For instance, the ball-milling process can enhance the homogeneity in the Y distribution of the NiCoCrAlY alloys to suppress S segregation at the interface during oxidation [39]. Since the size of the γ and β phases in the three alloys shows limited variation, the homogeneity of the RE distribution across these alloys can be considered to be nearly equivalent. However, after oxidation at 1200 ℃, oxide intrusions are observed at the interface between the oxide scale and NiCoCrAl-type EMPEAs. This observation shifts the focus to the differences in oxide intrusions among these alloys, which is the main subject of our investigation.

The oxide intrusions surrounding Y/Hf-rich oxides are predominantly distributed within the Al-depleted layer of the NiCoCrAl-type EMPEAs (Figs. 12–13). Given that the γ phase is Al-lean, the microstructure of the Al-depleted layer in the NiCoCrAl-type EMPEAs consists of the γ phase. Therefore, the distribution of oxide intrusions should be

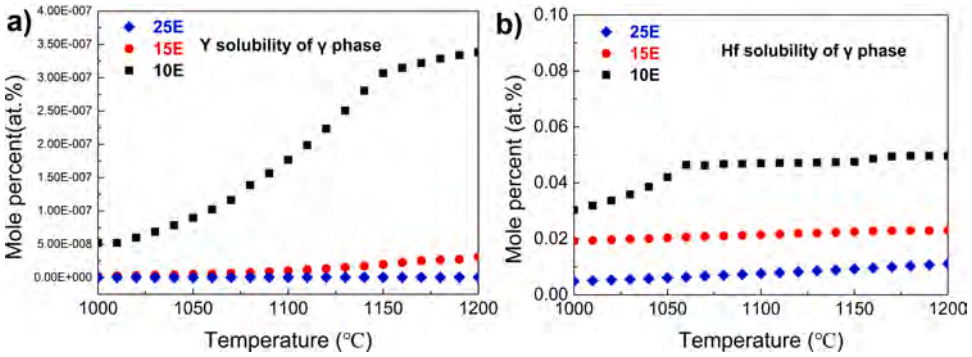

Fig. 19. Calculated Y and Hf solubility of the γ phase in NiCoCrAl-type EMPEAs at 1000–1200 ℃ using the TC software.

Table 9
Y and Hf solubility of the γ phase at 1200 ℃ calculated by the TC software.

Alloys	Y(at%)	Hf (at%)
25E	4.48×10^{-10}	0.011
15E	3.09×10^{-7}	0.023
10E	3.38×10^{-7}	0.050

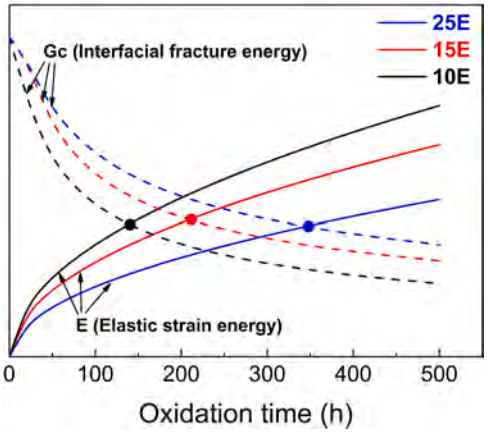

Fig. 20. Evolution of the elastic strain energy (solid lines) and interfacial fracture energy (dash lines) in the Al_2O_3 scale formed on the three alloys with oxidation time at 1200 ℃.

determined by the RE solubility of the γ phase. As shown in Fig. 19 and Table 9, the Hf solubility in the γ phase of NiCoCrAl-type EMPEAs decreases from ~ 0.050 at% of the 10E alloy to ~ 0.011 at% of the 25E alloy, while that of Y decreases from 3.38×10^{-7} to 4.48×10^{-10} at%. The thickness of the Al-depleted layer increases with time due to the ongoing consumption of Al to form the Al_2O_3 scale, consequently promoting the formation of RE-rich oxide at the scale/alloy interface. Moreover, compared to 10E alloy, the observation that fewer RE-rich precipitates are present in the 25E alloy after 100 h oxidation (Fig. S2), which can be attributed to its lower RE solubility in the γ phase. The higher Co and Cr concentrations reduce the solid solubility limit of Y and Hf in the γ phase, which means that a larger portion of REs remains in solid solution rather than precipitating out as secondary phases. As a result, there are fewer RE-rich precipitates to act as preferential sites for internal oxidation, leading to a less significant internal oxidation phenomenon in 25E alloy.

Hence, oxide intrusions surrounding the RE-rich oxides are found from the scale/alloy interface of 15E and 10E after oxidation for 100 h at 1200 °C on account of the higher solubility of the γ phase in these alloys. In contrast, the lower RE solubility in the γ phase of the 25E alloy reduces the likelihood of RE-rich oxide formation at the scale/alloy interface, thus leading to only minor oxide intrusions at the scale/alloy interface after oxidation for 500 h at 1200 °C. Other thing should be noted that the formation of RE-rich oxide inclusions in all three NiCoCrAl EMPEAs indicates that the current RE concentrations may exceed the optimal level, and further work is needed to optimize the RE effect for improved oxidation resistance.

In summary, increasing the Co and Cr concentrations in NiCoCrAl-type EMPEAs improves the interfacial fracture energy by lowering the RE solubility of the γ phase. The enhancement in interfacial fracture energy, in conjunction with a decrease of the driving force for scale spallation (elastic strain energy), contributes to the observed improvement in the spallation resistance. Fig. 20 presents the change of the driving force for scale spallation and interfacial fracture energy of the three alloys with oxidation time at 1200 ℃. The intersection of the elastic strain energy and interfacial fracture energy indicates the oxidation time when spallation of the Al_2O_3 scale occurs. Eventually, as the Co and Cr concentrations in the NiCoCrAl-type EMPEAs increase, the driving force for spallation decreases while the interfacial fracture energy increases, resulting in better spallation resistance.

5. Conclusions

The oxidation behavior of Y/Hf co-doped NiCoCrAl EMPEAs with different Co and Cr concentrations (25E, 15E, and 10E) is investigated at 1100 and 1200 °C to provide guidance on the development of oxidation-resistant NiCoCrAl alloys. Our results reveal that the NiCoCrAl-type EMPEAs designed by the CALPHAD method have an ultrafine lamellar and rod-like eutectic microstructure. The oxidation rate of the NiCoCrAl-type EMPEAs decreases with increasing Co and Cr concentrations at 1100 ℃ due to the enlarged columnar grain size, which results from the higher Hf solubility in the β phase. The higher Hf solubility delays the θ- to α-Al_2O_3 phase transformation in the β phase, thereby promoting larger columnar grains. The spallation resistance of the NiCoCrAl-type EMPEAs can be improved by increasing the Co and Cr concentrations at 1200 ℃ stemming from the reduction of the CTE and RE solubility of the γ phase. The reduction of CTE minimizes the residual stress in the oxide scale and decreases the driving force of spallation of the oxide scale. The smaller RE solubility in the γ phase lowers the propensity for oxide intrusion and formation at the scale/alloy interface, consequently increasing the interfacial fracture energy.

CRediT authorship contribution statement

Bingnan Qian: Methodology, Visualization. **Fangwei Guo:** Investigation, Methodology. **Paul K Chu:** Formal analysis, Writing – review & editing. **Xiaofeng Zhao:** Funding acquisition, Supervision. **Jie Lu:** Supervision, Writing – review & editing. **Aihui Huang:** Conceptualization, Data curation, Formal analysis, Writing – original draft. **Han Zhang:** Data curation, Formal analysis. **Xuanzhen Liu:** Formal analysis, Methodology. **Chao Yang:** Formal analysis, Writing – review & editing.

Declaration of Competing Interest

The authors declare that they have no known competing financial interests or personal relationships that could have appeared to influence the work reported in this paper.

Acknowledgments

This work was supported by the National Natural Science Foundation of China (Nos. 52201082, 52102072, and 51971139) and Shanghai Sailing Program (No. 22YF1419200). This work is also sponsored by the Chenguang Program supported by the Shanghai Education Development Foundation, Shanghai Municipal Education Commission (No. 21CGA10), and City University of Hong Kong Donation Research Grants (Nos. DON-RMG 9229021 and 9220061).

Appendix A. Supporting information

Supplementary data associated with this article can be found in the online version at doi:10.1016/j.corsci.2025.112944.

Data Availability

Data will be made available on request.

References

[1] N.P. Padture, M. Gell, E.H. Jordan, Thermal barrier coatings for gas-turbine engine applications, Science 296 (80) (2002) 280–284.
[2] S. Deng, P. Wang, Y. He, J. Zhang, Surface microstructure and high temperature oxidation resistance of thermal sprayed NiCoCrAlY bond-coat modified by cathode plasma electrolysis, J. Mater. Sci. Technol. 33 (2017) 1055–1060.
[3] H. Xu, J. Wu, – new materials, technologies and processes in thermal barrier coatings, in: H. Xu, H.B.T.-T.B.C. Guo (Eds.), Woodhead Publ. Ser. Met. Surf. Eng., Woodhead Publishing, 2011, pp. 317–328.
[4] WX. Wu, H.X. Liu, X.M. Jin, L.L. Guo, T. Zhu, L.B. Hu, C. Yang, P.H. Chen, C.J. Qiu, P.K. Chu, Unveiling high-temperature tribological behavior and wear mechanism of WCp/HEA composite coating via laser additive manufacturing, Ceram. Int. (2022), https://doi.org/10.1016/j.ceramint.2025.02.124.
[5] K. Yan, H. Guo, S. Gong, High-temperature oxidation behavior of beta-NiAl with various reactive element dopants in dry and humid atmospheres, Corros. Sci. 83 (2014) 335–342.
[6] D. Naumenko, B.A. Pint, W.J. Quadakkers, Current thoughts on reactive element effects in alumina-forming systems: in memory of John Stringer, Oxid. Met. 86 (2016) 1–43.
[7] M.J. Pomeroy, Coatings for gas turbine materials and long term stability issues, Mater. Des. 26 (2005) 223–231.
[8] C. Yang, C.Y. Wang, Z. Shen, L.P. Zhou, L.Y. Sheng, D.K. Xu, Y.F. Zheng, P.K. Chu, S. Xiao, T. Ying, X.Q. Zeng, Simultaneous improvement of wear and corrosion resistance of microarc oxidation composite coatings on ZK61 Mg alloy by doping with ZrO_2 nanoparticles, J. Mater. Sci. Technol. 224 (2025) 312–327.
[9] C.S. Tiwary, P. Pandey, S. Sarkar, R. Das, S. Samal, K. Biswas, K. Chattopadhyay, Five decades of research on the development of eutectic as engineering materials, Prog. Mater. Sci. 123 (2022) 100793.
[10] Y. Lu, Y. Dong, H. Jiang, Z. Wang, Z. Cao, S. Guo, T. Wang, T. Li, P.K. Liaw, Promising properties and future trend of eutectic high entropy alloys, Scr. Mater. 187 (2020) 202–209.
[11] Y. Lu, X. Gao, L. Jiang, Z. Chen, T. Wang, J. Jie, H. Kang, Y. Zhang, S. Guo, H. Ruan, Y. Zhao, Z. Cao, T. Li, Directly cast bulk eutectic and near-eutectic high entropy alloys with balanced strength and ductility in a wide temperature range, Acta Mater. 124 (2017) 143–150.
[12] J. Lu, H. Zhang, L. Li, Y. Chen, X. Liu, X. Zhao, F. Guo, Y hf co-doped $AlCoCrFeNi_{2.1}$ eutectic high-entropy alloy with excellent oxidation and spallation resistance under thermal cycling conditions at 1100 °C and 1200 °C, Corros. Sci. 187 (2021) 109515.
[13] J. Lu, H. Zhang, G. Ren, Y. Chen, L. Luo, H. Cai, X. Shan, X. Zhang, X. Zhao, A comparative study on the oxidation behavior and failure mechanisms of conventional NiCoCrAl alloy and in-situ composite $AlCoCrFeNi_{2.1}$ eutectic high-entropy alloy at 1300 °C, Compos. Part B Eng. 269 (2023) 111097.
[14] C. Bezençon, A. Schnell, W. Kurz, Epitaxial deposition of MCrAlY coatings on a Ni-base superalloy by laser cladding, Scr. Mater. 49 (2003) 705–709.
[15] K. Partes, C. Giolli, F. Borgioli, U. Bardi, T. Seefeld, F. Vollertsen, High temperature behaviour of NiCrAlY coatings made by laser cladding, Surf. Coat. Technol. 202 (2008) 2208–2213.
[16] L. Luo, X. Shan, Z. Zou, C. Zhao, X. Wang, A. Zhang, X. Zhao, F. Guo, P. Xiao, A high performance NiCoCrAlY bond coat manufactured using laser powder deposition, Corros. Sci. 126 (2017) 356–365.
[17] D. Duan, Y. Wu, H. Chen, X. Wang, X. Liu, H. Wang, S. Jiang, Z. Lu, A strategy to design eutectic high-entropy alloys based on binary eutectics, J. Mater. Sci. Technol. 103 (2022) 152–156.
[18] H. Jiang, K. Han, X. Gao, Y. Lu, Z. Cao, M.C. Gao, J.A. Hawk, T. Li, A new strategy to design eutectic high-entropy alloys using simple mixture method, Mater. Des. 142 (2018) 101–105.
[19] X. Jin, Y. Zhou, L. Zhang, X. Du, B. Li, A new pseudo binary strategy to design eutectic high entropy alloys using mixing enthalpy and valence electron concentration, Mater. Des. 143 (2018) 49–55.
[20] Q. Wu, Z. Wang, X. Hu, T. Zheng, Z. Yang, F. He, J. Li, J. Wang, Uncovering the eutectics design by machine learning in the Al–Co–Cr–Fe–Ni high entropy system, Acta Mater. 182 (2020) 278–286.
[21] C. Zhang, F. Zhang, S. Chen, W. Cao, Computational thermodynamics aided high-entropy alloy design, Jom 64 (2012) 839–845.
[22] A. Huang, Y. Chen, Z. Zhang, J. Shen, L. Li, X. Liu, H. Zhang, J. Lu, X. Zhao, Effect of Al content on the oxidation behavior of NiCoCrAlYHf alloys at 1100 °C, Corros. Sci. 222 (2023) 111417.
[23] R.J. Christensen, V.K. Tolpygo, D.R. Clarke, The influence of the reactive element yttrium on the stress in alumina scales formed by oxidation, Acta Mater. 45 (1997) 1761–1766.
[24] B.A. Pint, Optimization of reactive-element additions to improve oxidation performance of alumina-forming alloys, J. Am. Ceram. Soc. 86 (2003) 686–695.
[25] D. Young. High Temperature Oxidation and Corrosion of Metals, 2016.
[26] C. Wagner, Theoretical analysis of the diffusion processes determining the oxidation rate of alloys, J. Electrochem. Soc. 99 (1952) 369–380.
[27] H. Ren, R.R. Chen, T. Liu, X.F. Gao, G. Qin, S.P. Wu, J.J. Guo, Unraveling the oxidation mechanism of Y-doped AlCoCrFeNi high-entropy alloy at 1100 °C, Appl. Surf. Sci. 652 (2024) 159316.
[28] A. Gil, D. Naumenko, R. Vassen, J. Toscano, M. Subanovic, L. Singheiser, W. J. Quadakkers, Y-rich oxide distribution in plasma sprayed MCrAlY-coatings studied by SEM with a cathodoluminescence detector and Raman spectroscopy, Surf. Coat. Technol. 204 (2009) 531–538.
[29] B.A. Pint, Experimental observations in support of the dynamic-segregation theory to explain the reactive-element effect, Oxid. Met. 45 (1996) 1–37.
[30] T. Matsudaira, M. Wada, T. Saitoh, S. Kitaoka, Oxygen permeability in cation-doped polycrystalline alumina under oxygen potential gradients at high temperatures, Acta Mater. 59 (2011) 5440–5450.
[31] J.L. Smialek, N.S. Jacobson, B. Gleeson, D.B. Hovis, A. Heuer, Oxygen permeability and grain-boundary diffusion applied to alumina scales, NASA Tech. Memo. (2013).
[32] T.A. Ramanarayanan, M. Raghavan, R. Petkovic-Luton, The characteristics of alumina scales formed on Fe-based yttria-dispersed alloys, J. Electrochem. Soc. 131 (1984) 923–931.
[33] A.H. Heuer, D.B. Hovis, J.L. Smialek, B. Gleeson, Alumina scale formation: a new perspective, J. Am. Ceram. Soc. 94 (2011) s146–s153.
[34] H. Yu, R. Kasada, K. Inoue, S. Kondo, Y. Ogino, S. Ukai, Contribution of Y_2O_3/Hf co-doping to alumina scale growth on oxide dispersion strengthened Co-based superalloy, Corros. Sci. 227 (2024) 111775.
[35] M.W. Brumm, H.J. Grabke, The oxidation behaviour of NiAl-I. Phase transformations in the alumina scale during oxidation of NiAl and NiAl-Cr alloys, Corros. Sci. 33 (1992) 1677–1690.
[36] C. Yang, T. Ying, A.H. Huang, J. Huang, P.H. Chen, P.K. Chu, X.Q. Zeng, Enhancing the corrosion resistance of MAO coatings on LY12 alloy by in situ co-doping with zinc phosphate and cerium phosphate, Corros. Commun 17 (2025) 35–43.
[37] H. Yu, S. Kondo, R. Kasada, S. Ukai, Influence of Ni content on the oxidation behavior of alumina-forming Co-based oxide dispersion strengthened superalloys at 900 °C, Corros. Sci. 212 (2023) 1–14.
[38] Y. Chen, X. Zhao, P. Xiao, Effect of microstructure on early oxidation of MCrAlY coatings, Acta Mater. 159 (2018) 150–162.
[39] B.A. Pint A, J.R. Martin, L.W. Hobbs, The oxidation mechanism of θ-Al_2O_3 scales, Solid State Ion. 78 (1995) 99–107.
[40] C. Zhao, Y. Zhou, Z. Zou, L. Luo, X. Zhao, F. Guo, P. Xiao, Effect of alloyed Lu, Hf and Cr on the oxidation and spallation behavior of NiAl, Corros. Sci. 126 (2017) 334–343.
[41] J. Lu, Y. Chen, C. Zhao, H. Zhang, L. Luo, B. Xu, X. Zhao, F. Guo, P. Xiao, Significantly improving the oxidation and spallation resistance of a MCrAlY alloy by controlling the distribution of yttrium, Corros. Sci. 153 (2019) 178–190.
[42] Y. Niu, X.J. Zhang, Y. Wu, F. Gesmundo, The third-element effect in the oxidation of Ni–xCr–7Al (x = 0, 5, 10, 15 at%) alloys in 1 atm O2 at 900–1000 °C, Corros. Sci. 48 (2006) 4020–4036.
[43] Y. Huang, X. Peng, X.Q. Chen, The mechanism of θ- to α-Al2O3 phase transformation, J. Alloy. Compd. 863 (2021) 158666.
[44] R. Raggio, G. Borzone, R. Ferro, The Al-rich region in the Y–Ni–Al system: microstructures and phase equilibria, Intermetallics 8 (2000) 247–257.
[45] J. Huang, B. Yang, H. Chen, H. Wang, Thermodynamic optimisation of the Ni-Al-Y ternary system, J. Phase Equilibr. Diffus 36 (2015) 357–365.
[46] S. Guo, C. Ng, J. Lu, C.T. Liu, Effect of valence electron concentration on stability of fcc or bcc phase in high entropy alloys, J. Appl. Phys. 109 (2011).
[47] Y. Zhang, T.T. Zuo, Z. Tang, M.C. Gao, K.A. Dahmen, P.K. Liaw, Z.P. Lu, Microstructures and properties of high-entropy alloys, Prog. Mater. Sci. 61 (2014) 1–93.
[48] W.R. Wang, W.L. Wang, J.W. Yeh, Phases, microstructure and mechanical properties of $Al_xCoCrFeNi$ high-entropy alloys at elevated temperatures, J. Alloy. Compd. 589 (2014) 143–152.

[49] T. Xu, S. Faulhaber, C. Mercer, M. Maloney, A. Evans, Observations and analyses of failure mechanisms in thermal barrier systems with two phase bond coats based on NiCoCrAlY, Acta Mater. 52 (2004) 1439–1450.
[50] J. Lu, L. Li, Y. Chen, X. Liu, X. Zhao, F. Guo, P. Xiao, Y hf co-doped AlCoCrFeNi high-entropy alloy coating with superior oxidation and spallation resistance at 1100 °C, Corros. Sci. 182 (2021) 109267.
[51] L. Qiu, F. Yang, W. Zhang, X. Zhao, P. Xiao, Effect of Al content on the lifetime of thermally grown oxide formed on Ni-Al alloys after isothermal oxidation, Corros. Sci. 89 (2014) 13–20.
[52] V.K. Tolpygo, J.R. Dryden, D.R. Clarke, Determination of the growth stress and strain in α-Al_2O_3 scales during the oxidation of Fe-22Cr-4.8Al-0.3Y alloy, Acta Mater. 46 (1998) 927–937.
[53] J.A. Haynes, B.A. Pint, W.D. Porter, I.G. Wright, Comparison of thermal expansion and oxidation behavior of various high-temperature coating materials and superalloys, Mater. High Temp. 21 (2004) 87–94.
[54] M.J. Pomeroy, Coatings for gas turbine materials and long term stability issues, Mater. Des. 26 (2005) 223–231.
[55] P. Hancock, J.R. Nicholls, Fundamental and engineering aspects of coatings for diesel and gas turbine engineering, in: NATO Adv. Work. Coatings Heat Engines, 1st, n.d.
[56] A. Huang, L. Li, X. Liu, H. Zhang, M. Li, X. Zhang, J. Lu, X. Zhao, Superior oxidation resistance of a YHf co-doped $Al_{18}Co_{30}Cr_{10}Fe_{10}Ni_{32}$ eutectic high-entropy alloy at 1100–1300 °C, J. Alloy. Compd. 992 (2024) 174597.
[57] J.W. Hutchinson, M.Y. He, A.G. Evans, Influence of imperfections on the nucleation and propagation of buckling driven delaminations, J. Mech. Phys. Solids 48 (2000) 709–734.
[58] V.K. Tolpygo, D.R. Clarke, Alumina scale failure resulting from stress relaxation, Surf. Coat. Technol. (1999) 1–7.

Oxidation behavior and failure mechanism of NiCoCrAl eutectic multi-principal element alloys co-doped with Y and Hf at 1100 ℃ and 1200 ℃

Aihui Huang [a], Chao Yang [b,*], Xuanzhen Liu [a], Han Zhang [a], Fangwei Guo [a], Bingnan Qian [c], Jie Lu [a,*], Xiaofeng Zhao [a], Paul K. Chu [d]

[a] Shanghai Key Laboratory of Advanced High-Temperature Materials and Precision Forming, School of Materials Science and Engineering, Shanghai Jiao Tong University, Shanghai, 200240, China

[b] National Engineering Research Center of Light Alloy Net Forming, Shanghai Jiao Tong University, China

[c] National Key Laboratory of Nuclear Reactor Technology, Nuclear Power Institute of China, Chengdu, 610213, China

[d] Department of Physics, Department of Materials Science & Engineering, and Department of Biomedical Engineering, City University of Hong Kong, Tat Chee Avenue, Kowloon, Hong Kong, China

[*] Corresponding authors: Chao Yang (chaoyang0315@163.com); Jie Lu (lu-jie@sjtu.edu.cn)

Section 1 DSC analysis

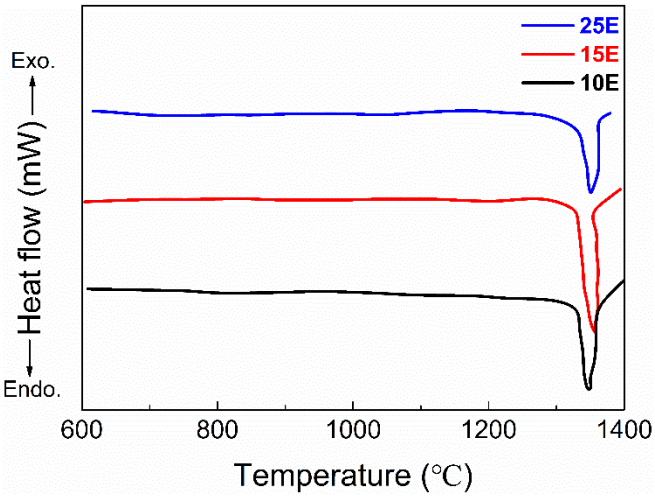

Fig. S1 DSC heat curves of NiCoCrAl EMPEAs, revealing a single endothermic peak during heating.

Section 2 The distribution of Y/Hf-rich precipitates after 100 h oxidation at 1200 ℃

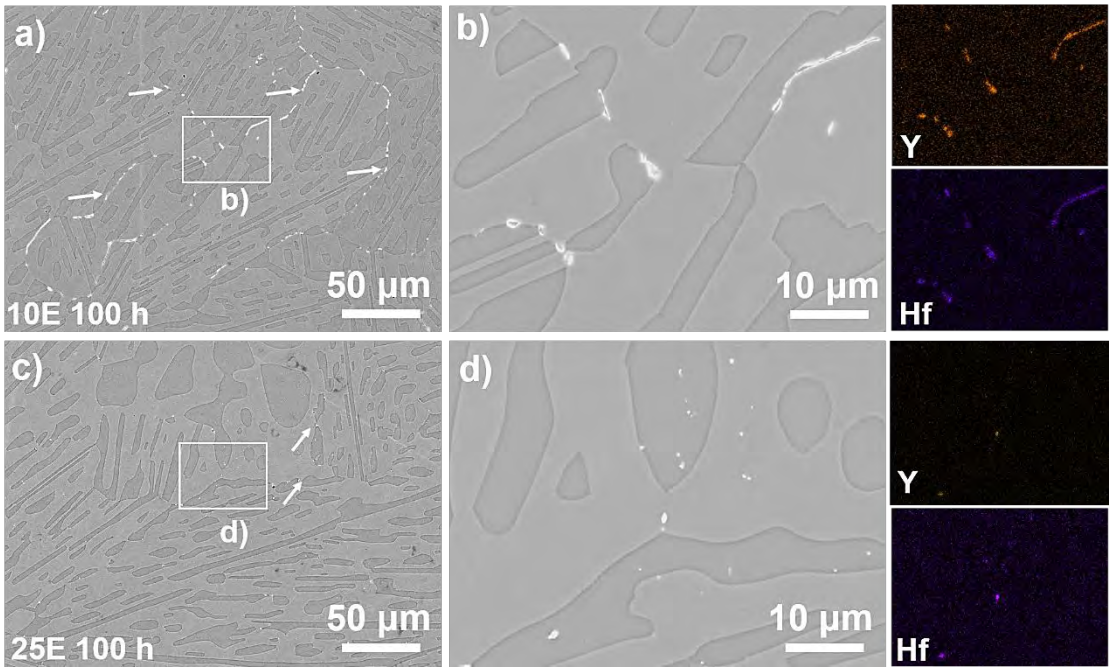

Fig. S2 The microstructure of 10E and 25E alloy after 100 h oxidation at 1200 ℃: a, c) low magnification BSE images, showing the overview of microstructure in 10E and 25E alloys (white arrows indicates the Y/Hf-rich precipitates); b, d) high magnification BSE images and corresponding EDS mapping, showing the detail of Y/Hf-rich precipitates.

Fig. S2 shows the distribution of Y/Hf-rich precipitates in 10E and 25E alloy after 100 h oxidation at 1200 ℃. In the 10E alloy, Y/Hf-rich precipitates are predominantly located at grain boundaries, showing a strong preference on the γ phase. In contrast, the 25E alloy exhibits a more uniform distribution of Y/Hf-rich precipitates across both its γ and β phases, without a notable tendency for aggregation. Furthermore, the phase size of the Y/Hf-rich precipitates in the 25E alloy is significantly larger compared to that in the 10E alloy. These results indicate that the distribution of Y/Hf precipitates plays important role on the difference of oxide intrusions in the NiCoCrAl EMPEAs.

Section 3 The thickness of Al_2O_3 scale after 250 h oxidation at 1200 ℃

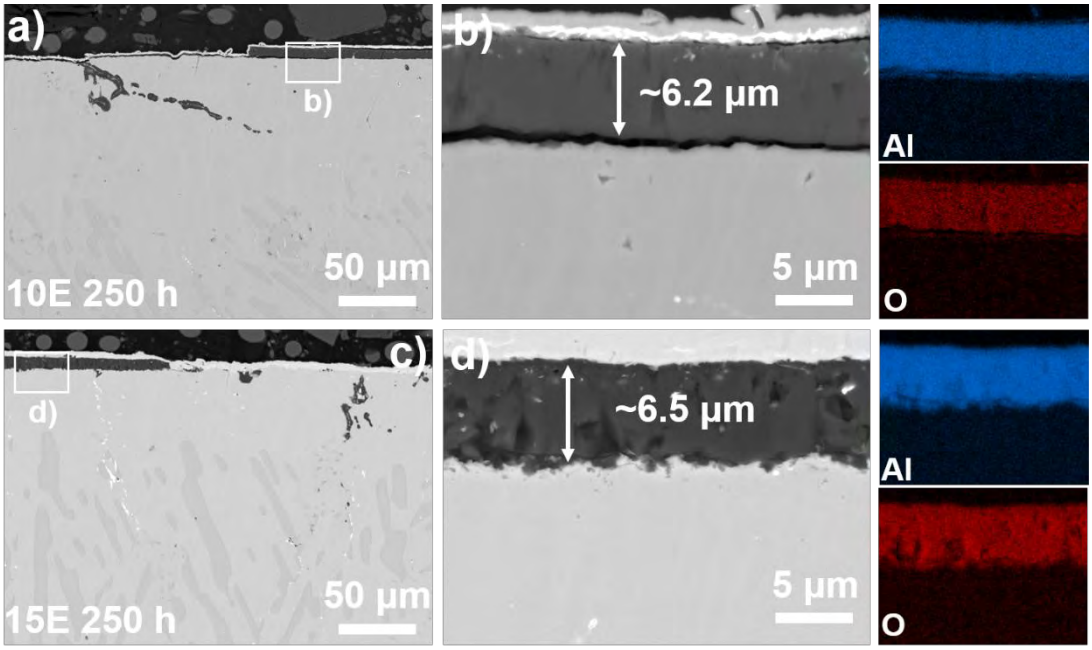

Fig. S3 The cross-sectional morphology of Al_2O_3 scale formed on the 10E and 15E alloys after 250 h oxidation at 1200 ℃: a, c) low magnification BSE images, showing the overview of Al_2O_3 scale; b, d) high magnification BSE images and corresponding EDS mapping, showing the thickness of Al_2O_3 scale.